crystals

MDPI

Article

Effect of Electrochemical Hydrogen Charging on Blistering and Mechanical Properties Behavior of Q690 Steel

Heng Ma [1], Huiyun Tian [2,*], Zhongxue Wang [3], Kang He [1], Yuexiang Wang [1], Qingpu Zhang [1], Deyun Liu [2] and Zhongyu Cui [2]

[1] Yinshan Section Steel Corporation of Laiwu Steel Group Ltd., Jinan 271104, China
[2] School of Materials Science and Engineering, Ocean University of China, Qingdao 266100, China; cuizhongyu@ouc.edu.cn (Z.C.)
[3] Shandong Iron & Steel Corporation Ltd., Jinan 271104, China
* Correspondence: tianhuiyun@ouc.edu.cn; Tel.: +86-178-6427-2237

Abstract: The purpose of this work is to study the effect of charging conditions on hydrogen damage. The effects of electrochemical hydrogen charging current density and time on hydrogen-induced blistering (HIB), cracking behavior, and mechanical properties of Q690 steel are studied by electrochemical hydrogen charging, microstructure observation, and slow strain rate tensile (SSRT) tests. The results show that HIB and internal cracks occur when the Q690 steel is charged at different current densities. The charging conditions have a significant effect on the HIB characteristics of the material and the morphology, number, size, and location of internal cracks. The geometrical parameters of blisters on the surface of Q690 steel are quantitatively evaluated, and deeper cracks are found at higher hydrogen concentrations. At high hydrogen charging current density (50 mA/cm^2), due to the accumulation of a large number of hydrogen atoms and the precipitation of hydrogen, the active sites on Q690 steel surface increase dramatically, leading to the initiation of a large number of blisters. At this time, high current density is responsible for the initiation of blisters. The relationship between hydrogen charging current density and mechanical properties of Q690 steel is studied, and the change in the fracture morphology is observed. The Q690 steel was damaged and failed due to an internal crack caused by excessive hydrogen pressure. On the other hand, electrochemical hydrogen charging leads to the degradation of mechanical properties and the transition from ductile fracture to brittle fracture.

Keywords: low-alloy steel; hydrogen blister; hydrogen-induced cracking; fracture behavior; electrochemical hydrogen

Citation: Ma, H.; Tian, H.; Wang, Z.; He, K.; Wang, Y.; Zhang, Q.; Liu, D.; Cui, Z. Effect of Electrochemical Hydrogen Charging on Blistering and Mechanical Properties Behavior of Q690 Steel. *Crystals* **2023**, *13*, 918. https://doi.org/10.3390/cryst13060918

Academic Editor: Umberto Prisco

Received: 17 May 2023
Revised: 30 May 2023
Accepted: 2 June 2023
Published: 7 June 2023

1. Introduction

With the development of marine equipment, 690 MPa marine low-alloy steel has been widely used [1,2]. However, due to the excessive cathodic protection, 690 MPa steel tends to absorb hydrogen in the service environment and is prone to hydrogen-assisted degradation [3,4].

Ćwiek [5] indicated that one of the important factors affecting HIC sensitivity is the content of H in the steel. In general, HIC sensitivity increases with the increase in H content. Zhou et al. [6] reported that stable austenitic twinned plastic steels are sensitive to hydrogen embrittlement after being charged with hydrogen at a high-pressure hydrogen environment. Our previous work has also confirmed that H leads to increased SCC sensitivity of steel by penetrating and diffusing the interior of E690 steel [7]. Depover et al. [8] and Venezuela et al. [9] pointed out that the more H trapping sites there are in steel, the more likely HIC occurs. Ma et al. [10] confirmed that the SCC of E690 steel in the seawater environment increases due to H-induced brittle fracture with the increase in cathodic potential. Wu et al. [11] argued that a sharp rise in hydrogen permeation current led to a significant increase in the comprehensive loss rate for X80 steel. Our previous work also indicated

that the cathodic potential changed the interfacial pH value so that significant changes in hydrogen diffusion and permeation behavior influenced the change in the preferential cracking pathway of the E690 steel [12]. However, calcareous deposits are easily formed on the steel surface after applying the cathodic potential in artificial seawater, which attaches to the steel surface. Deslouis et al. [13] and Barchiche et al. [14] confirm this result. The attachment of calcareous deposits affects hydrogen behavior [15,16]. The applied cathodic potential also produces a certain cathodic current. The change of hydrogen concentration on the steel surface can be quantified by cathodic current density. Therefore, we studied the effect of electrochemical hydrogen charging on blistering and mechanical property loss of Q690 steel using hydrogen charging current.

On the other hand, hydrogen charging time is another important factor of hydrogen damage. Hydrogen charging time directly affects the accumulation of hydrogen at the active site. Li et al. [17] found that an increase in charging time leads to a change in hydrogen damage morphology. After 40 h of hydrogen charging, the toughness of the titanium alloy suffered a significant loss, and the elongation decreased from 20.2% to 1.0% [18]. As the electrochemical hydrogen charging current density increases, the HE sensitivity of pipeline steel and girth weld increases [19]. Therefore, the correlation of electrochemical hydrogen charging current density and hydrogen charging time with blistering and mechanical properties' loss of Q690 steel was investigated by applying hydrogen charging current density.

In the absence of external load, hydrogen-induced cracking (HIC) and blistering are considered to be the main factors that threaten the safety of steel in service [20–22]. When the hydrogen concentration in the material reaches a critical value, atomic hydrogen recombines into molecular gaseous hydrogen at hydrogen traps (material defects such as inclusions, grain boundaries, dislocations, and hard phase components) [23], and cannot migrate further, leading to the local formation of high internal pressure. As the internal pressure gradually increases, crack propagation occurs even when no external loading is applied. When a crack forms on the surface of the material, the resulting pressure pushes the material outward, causing a dome-shaped bump on the surface of the material called a hydrogen-induced blister (HIB) [24,25]. The location and characteristics of blistering in charged steel have been extensively studied in the published literature [25–27]. Extensive work suggests that inclusions and secondary phases in steel are the main inspiration sites for blisters [25,28]. The existence of hydrogen in voids or microcracks promoted the propagation of hydrogen-induced cracks [29]. During electrochemical hydrogen charging, higher current density and longer charging time lead to a rapid increase in the diameter and density of blisters [24,28]. The blistering can occur in X80 steel when the current density reaches the critical value, but the shape of the blister changes as the current density increases further [21].

The resulting hydrogen damage naturally reduces the overall mechanical properties (such as toughness, strength, and fatigue property) of the charged steel, a phenomenon known as hydrogen embrittlement (HE) [30]. The formation of hydrogen damage leads to a decrease in yield strength, an increase in embrittlement factor and area, and finally contributes to the early failure of the steel [31]. After 40 h of hydrogen charging, the toughness of the titanium alloy suffered a significant loss, and the elongation decreased from 20.2% to 1.0% [18]. As the hydrogen charging current density increases, the HE sensitivity of pipeline steel and girth weld increases [19].

Even though there are some works about the hydrogen damage of different materials, the hydrogen-related deterioration of Q690 steel is rather scarce. Therefore, the charging of Q690 steel with different charging current densities and charging times is used in this work to illustrate the evolution of hydrogen damage on the surface and inside of the sample. In addition, the effect of the charging current density on the mechanical properties (elongation and tensile strength values, and HE susceptibility) of Q690 steel is analyzed.

2. Material and Methods

2.1. Material

The Q690 steel was used as the experimental material in this work. The chemical composition of the Q690 steel is provided in Table 1, along with the calculated Cr_{eq} and Ni_{eq} based on the alloying elements.

Table 1. Chemical composition of base material and welding material.

Material	C	Si	Mn	Cr	Ni	Mo	Cr_{eq}	Ni_{eq}	Fe
Q690	0.14	0.035	1.31	0.51	0.02	0.13	0.91	5.90	Bal.

2.2. Hydrogen Charging Test

The Q690 steel was electrochemically charged with hydrogen in 0.5 M H_2SO_4 + 3 g/L CH_4N_2S (NH_4SCN) solution. Samples (dimensions of 10 × 10 × 2 mm^3) were gradually ground to 1500 # with grit SiC paper, then ultrasonically vibration cleaned in ethanol, and dried in cold air. Hydrogen charging specimens were sealed in epoxy resin, leaving a working area of 1 cm^2. The sample was connected to a cathode, and a platinum sheet was used as the anode. A saturated calomel electrode was used as the reference electrode. A schematic diagram of the experimental setup for hydrogen charging is shown in Figure S1 in the Supporting Information. The Q690 steel was charged with different current densities (2, 5, 10, and 50 mA/cm^2) and charging times (1, 3, 6, and 12 h) at 22 ± 2 °C. After hydrogen charging, the bulges on the surface of the sample were observed by a confocal laser scanning microscopy (CLSM, Keyence VK-X250, Osaka, Japan) to determine their shape, number, and size distribution. The cross-sections were analyzed by scanning electron microscopy (SEM) to collect information about the morphology and cracking pathway of internal cracks in the hydrogen-charged specimens. The relevant parameters of hydrogen charging experiments are shown in Table S1 in the Supporting Information.

2.3. Slow Strain Tensile Test

The hydrogen embrittlement (HE) behavior of Q690 steel under electrochemical hydrogen charging was studied by the slow strain rate tensile test (SSRT) at room temperature. The tensile specimen was cut from the steel sheet perpendicular to the rolling direction (Figure S2a in the Supporting Information) according to GB/T 15970.7. The tensile direction of the specimen had the highest-stress corrosion cracking (SCC) sensitivity [32]. The sample size used for the SSRT experiment and the schematic diagram of the SSRT experiment process is shown in Figure S2b,c in the Supporting Information. The middle of the sample was left 20 mm exposed to the test solution, and the remaining surface was sealed with silica gel. All the SSRT experiments were performed at room temperature with a constant strain rate of 10^{-6} s^{-1}. Before the test, the samples were immersed in the solution with current densities of 2, 5, 10, and 50 mA/cm^2 for 12 h, and the current density was applied continuously during the tensile process. Each set of tensile tests was performed at least three times to check for repeatability.

The HE susceptibility was calculated by the toughness loss [33]:

$$I_\delta = \left(1 - \frac{\delta_c}{\delta_0}\right) \times 100\% \quad (1)$$

where δ_c and δ_0 are the fracture strain in solutions and air. After removing the surface corrosion products, the fracture morphology of the tensile specimen was observed by SEM.

3. Results and Discussion

3.1. HIB Analysis

Figure 1 shows the macroscopic surface morphologies of the Q690 alloy after charging for 12 h at different current densities. The surfaces at the four current densities are covered

with blisters, which have an almost elliptical shape and are generated from the surface of the steel. With the increase in the current density, the number of blisters increases, and the shape also changes significantly. At low current densities, the blister shape exhibits a well-defined dome (Figure 1a–c). As the current density increases, the blister shape also changes to a flat-topped shape and a low plateau-like elevation with ragged edges (Figure 1d). The above results show that the hydrogen damage mechanism of Q690 steel has changed under high current density (10 mA/cm^2 and 50 mA/cm^2). At low current densities (2 mA/cm^2 and 5 mA/cm^2), the crack propagation path is dominated by internal hydrogen pressure, while high-angle grain boundaries become the dominant crack path as the current density increases [17].

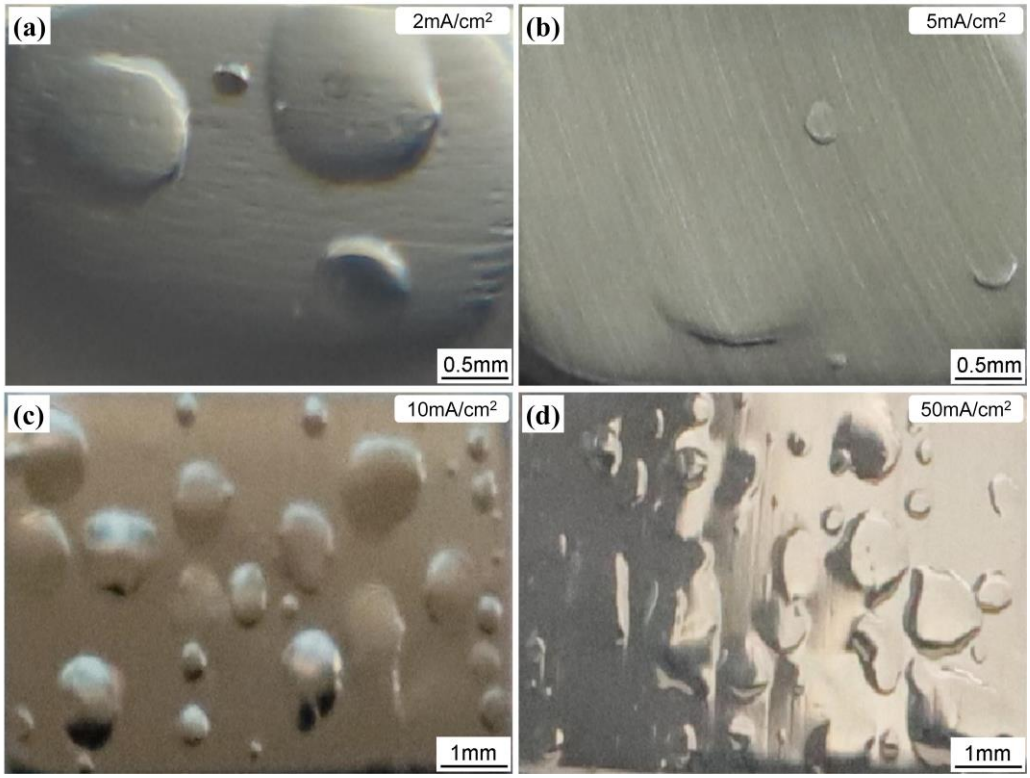

Figure 1. Surface morphologies of Q690 steel after charging for 12 h at different hydrogen charging current densities: (**a**) 2 mA/cm^2; (**b**) 5 mA/cm^2; (**c**) 10 mA/cm^2; (**d**) 50 mA/cm^2.

Figure 2 provides 3D profiles of blisters at different hydrogen charging current densities and times. No HIB occurs after 3 h of electrochemical hydrogen charging at current densities of 2 and 5 mA/cm^2. With the increase in time, small dome-like blisters appear after 6 h of hydrogen charging, and large blisters appear after 12 h (Figure 2a_1,a_2,b_1,b_2). At a hydrogen charging current density of 10 mA/cm^2, aggregated and small blisters appear after 1 h of hydrogen charging, and the blisters gradually increase with the increase in time (Figure 2c_1–c_4). Larger blisters are generated at a hydrogen charging current density of 50 mA/cm^2 for just over 1 h of hydrogen charging (Figure 2d_1). After 12 h, a blister cap forms, with some small blisters superimposed on the larger blisters and a distinct crack at the top of the blisters. The tensile stress and deformation are the maximum at the highest point of the blisters, which are responsible for the formation of cracks [17].

In general, with the extension of hydrogen charging time, the blisters grow and the proportion of larger-size blisters increases (Figure 3a–d). At the current density of 50 mA/cm^2, the surface of the sample is dominated by blisters below 20 μm, which indicates that HIB is more inclined to initiate at a high current density (50 mA/cm^2). The number of blisters increases with the increasing hydrogen charging time and current density (Figure 3e). The maximum diameter of the blisters in different hydrogen charging

environments is shown in Figure 4. The maximum blister diameter increases with the increase in hydrogen charging time. At 1 h of hydrogen charging, the size of the blister increases with the current density. However, the opposite result is shown at 12 h of hydrogen charging. For the hydrogen charging time of 3 h and 6 h, the blister size increases and then decreases.

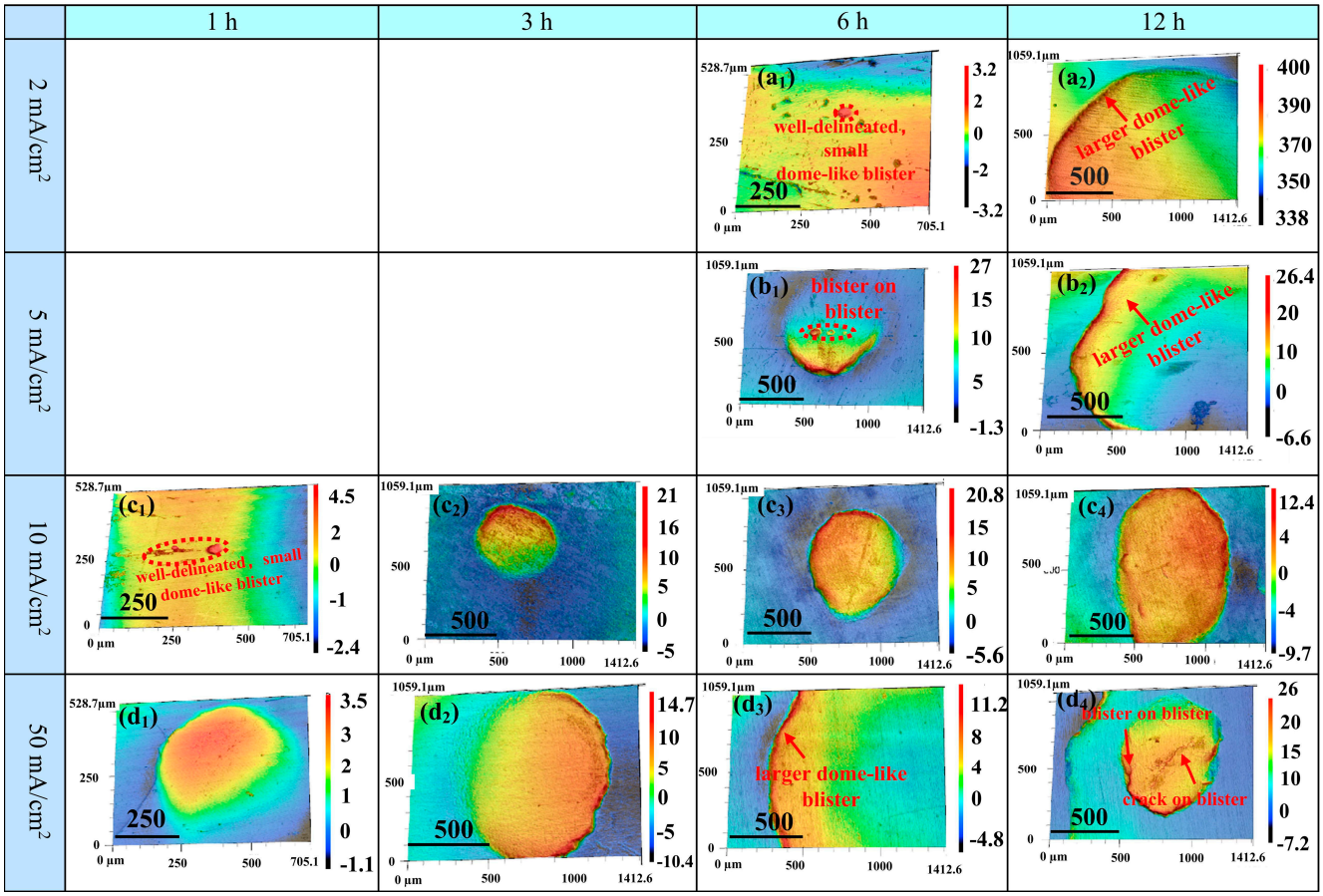

Figure 2. CLSM height maps of blisters after hydrogen charging for different times at different current densities. ((**a1**)—2 mA/cm^2 at 6 h; (**a2**)—2 mA/cm^2 at 12 h; (**b1**)—5 mA/cm^2 at 6 h; (**b2**)—5 mA/cm^2 at 12 h; (**c1**)—10 mA/cm^2 at 1 h; (**c2**)—10 mA/cm^2 at 3 h; (**c3**)—10 mA/cm^2 at 6 h; (**c4**)—10 mA/cm^2 at 12 h; (**d1**)—50 mA/cm^2) at 1 h; (**d2**)—50 mA/cm^2 at 3 h; (**d3**)—50 mA/cm^2 at 6 h; (**d4**)—50 mA/cm^2 at 12 h).

When the electrochemical hydrogen charging time is relatively short (1 h), the maximum diameter of blisters also increases with the increase in the hydrogen charging current density (Figure 4), which proves that the hydrogen charging current density affects the growth of blisters. When the hydrogen charging time is long (12 h), the opposite results appear (Figure 4), which proves that the hydrogen charging current density affects the initiation of blisters. As the charging current density increases, the number of blisters increases (Figure 3e), which also confirms that the hydrogen charging current density dominates the blistering initiation.

When the hydrogen charging current is constant, the maximum diameter of blisters increases with the prolongation of hydrogen charging time (Figure 4), which confirms that the growth of blisters is related to hydrogen charging time. At the same time, the number of blisters also increases (Figure 3e), confirming that the initiation of blisters is also related to the hydrogen charging time (Figure 3e).

In summary, the current density mainly affects the initiation of blistering when the hydrogen charging time is long (12 h). At a certain hydrogen charging current density,

the hydrogen charging time affects the growth and initiation of blisters. The formation of blisters is generally related to the electrochemical hydrogen charging conditions. Both the current density and the hydrogen charging time affect the diameter and number of blisters [17,28], and further alter the blister characteristics [34]. During the hydrogen charging process, the hydrogen ions on the cathodic surface are reduced to hydrogen atoms [17]:

$$2H^+ + 2e^- \rightarrow 2H(\text{atomic hydrogen}) \rightarrow H_2(\text{gas}) \quad (2)$$

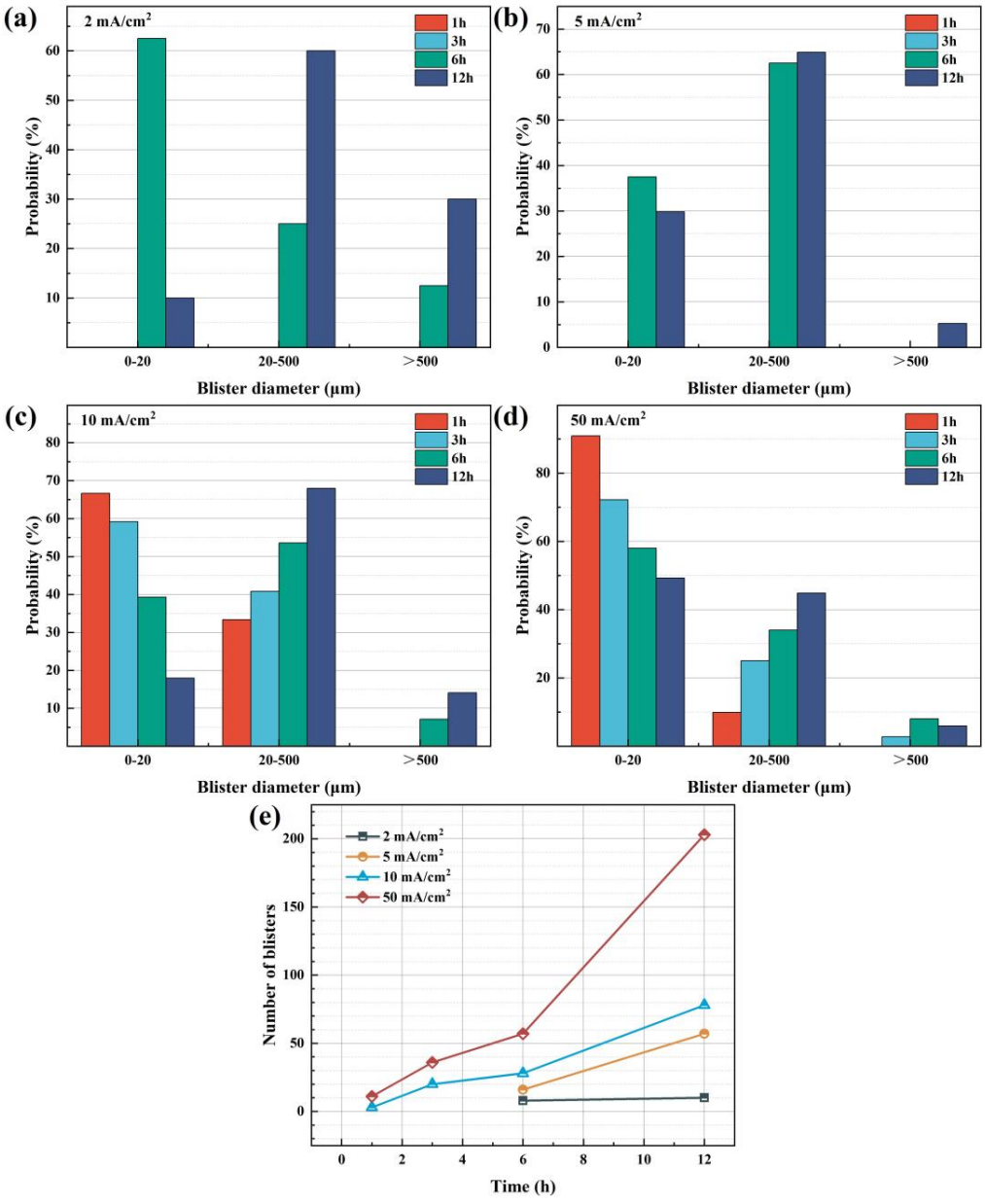

Figure 3. The diameter distribution ((**a**)—2 mA/cm^2; (**b**)—5 mA/cm^2; (**c**)—10 mA/cm^2; (**d**)—50 mA/cm^2) and number (**e**) of blisters in Q690 steel after hydrogen charging.

Part of the hydrogen atoms are absorbed and dissolved near the sample surface, and the other part is released as hydrogen gas. The increase in charge time results in a rise in the pressure of the gas in the cavity, leading to the formation of a surface HIB and internal cracks. Longer electrochemical hydrogen charging time (12 h) results in higher hydrogen content, which induces more hydrogen damage [35]. In a short charging time (1 h), the hydrogen content in the matrix is less, and no obvious hydrogen damage is found on the

surface of the sample at a low current density (2 mA/cm^2) (Figure 2). As the charging time increases, more blisters are activated, thus increasing the number of HIB. Greater current density leads to a higher driving force and a higher solubility of hydrogen in the substrate [36]. Under the condition of the greater driving force and longer charging time (12 h), the hydrogen content in the matrix further increases and the hydrogen damage is aggravated.

An internal void near the surface of Q690 steel filled with high-pressure hydrogen gas was observed on the surface, causing the surface to bulge [37], which is consistent with the findings of Zhang et al. [21]. The hydrogen bubble growth process can be divided into three stages: nucleation, growth, and rupture. Hydrogen atoms diffuse into voids, inclusions, or near other active sites within the sample. The classic hydrogen-enhanced decohesion model (HEDE) shows that hydrogen reduces the cohesive force between atoms at the interface [38,39]. Robertson et al. [39–41] proposed the synergistic mechanism between HEDE and hydrogen-enhanced local plasticity (HELP). The crack process is the reduction of the decohesion force between atoms, and the condition for achieving the reduction is hydrogen-induced local plasticity, which also confirmed the emergence of the blisters phenomenon. When the internal pressure at the hydrogen accumulation site reaches the yield strength of the material, blisters and cracks may occur by the deformation of the material. As the hydrogen concentration continues to increase and exceeds the material's atomic decohesion force, cracks begin to nucleate and expand at the surface [21,24]. At this time, blisters appear on the macroscopic surface. When the pressure inside the blisters is too high, the bubble ruptures.

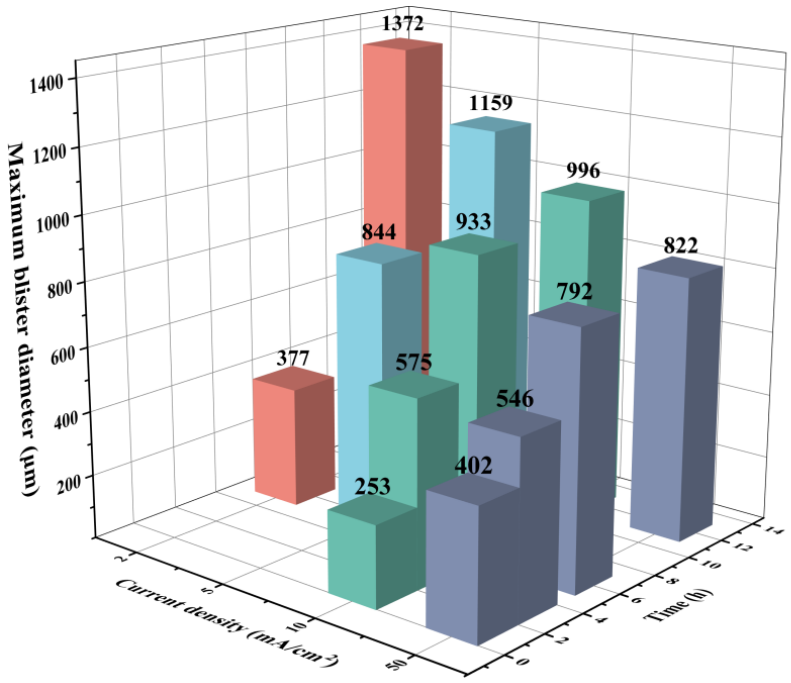

Figure 4. The maximum blister diameter on Q690 steel as a function of the charging time and current density.

There is a close relationship between surface blisters and internal cracks. The cross-sections are analyzed to better assess the hydrogen damage as a function of current density (Figure 5). It can be seen that electrochemical hydrogen charging causes surface blisters and internal cracks. Most of the cracks are located near the surface, mainly in the form of concave stepped cracks, and the cracks are mainly transgranular and intergranular. The width of deeper cracks in the sample is smaller than those under the surface blisters, which are mainly intergranular cracks, which may be related to the higher hydrogen concentration [12]. It can be seen that only at a larger current density (50 mA/cm^2), or with

a longer period of continuous hydrogen charging (12 h), small hydrogen-induced cracks appear in the deeper interior of the sample. The above results confirm the interface cracking when hydrogen concentration is high [12]. If the hydrogen charging current density is small (2 mA/cm^2) or the hydrogen charging time is short (1 h), there is enough time for hydrogen to diffuse to the phase interface and aggregate, resulting in the coexistence of transgranular and intergranular cracking. When the electrochemical hydrogen charging current density is too high (50 mA/cm^2) or the electrochemical hydrogen charging time is too long (12 h), hydrogen is more likely to accumulate and diffuse in the large angle grain boundary (primary austenite grain boundary), resulting in cracking mainly along the grain boundary.

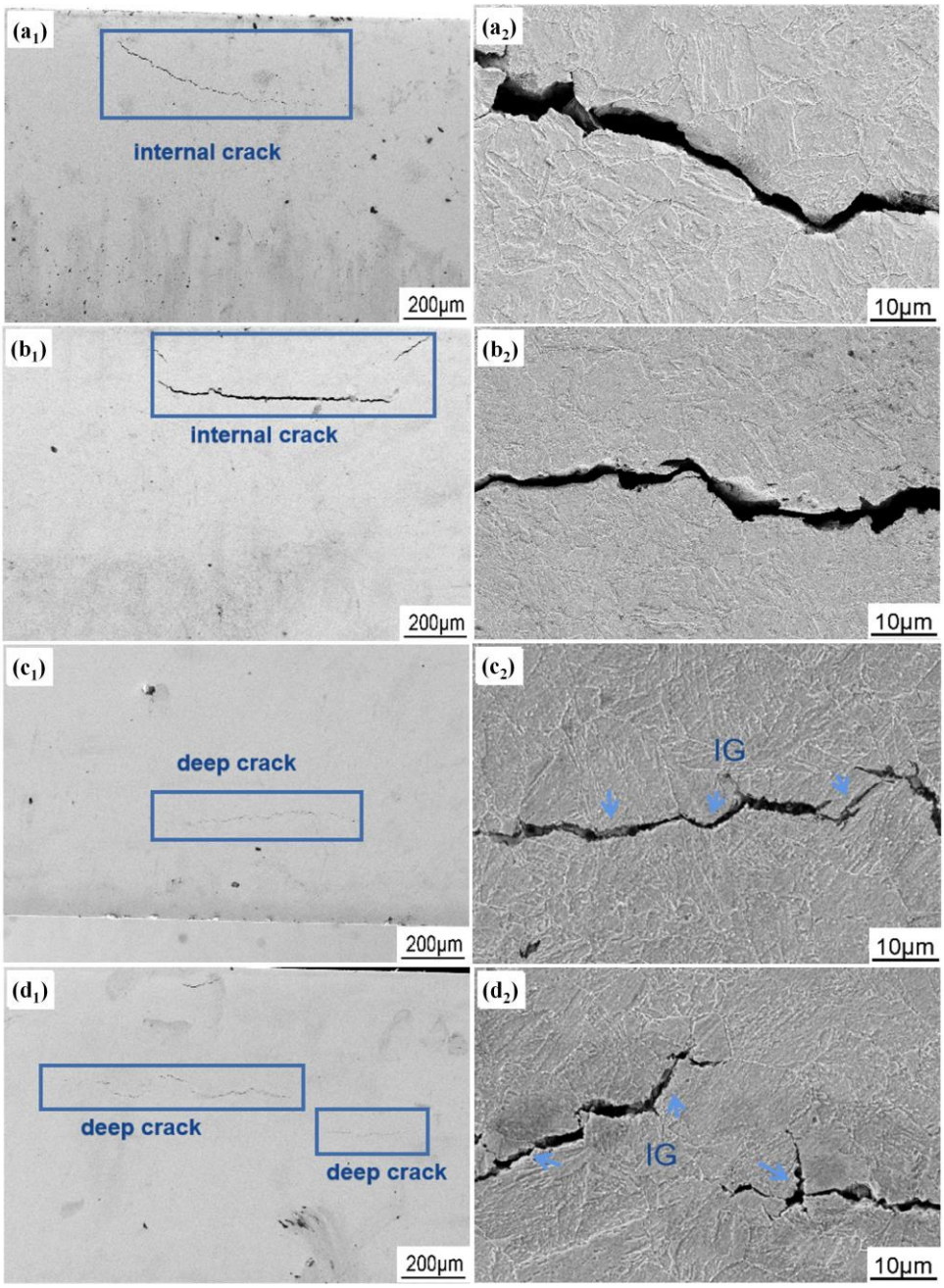

Figure 5. Morphology and cracking pathway of Q690 substrate under bubbles after hydrogen charging at current densities of 2 mA/cm^2 (**a$_1$**,**a$_2$**), 5 mA/cm^2 (**b$_1$**,**b$_2$**), 10 mA/cm^2 (**c$_1$**,**c$_2$**), and 50 mA/cm^2 (**d$_1$**,**d$_2$**) for 12 h. ("deep crack" refers to the crack that appears in the specimen further away from the hydrogen-charging surface).

3.2. Stress Corrosion Cracking

3.2.1. Mechanical Properties Analysis

Figure 6 shows the results of the tensile test including strain–stress curves, elongation and tensile strength values, and HE susceptibility of the Q690 steel after charging at different current densities. As you can see from Figure 6, the ductility and tensile strength of the charged samples at room temperature are lower than those of the uncharged steel (Figure 6a,b). The sample is affected by hydrogen, resulting in a loss of mechanical properties [42]. The ultimate tensile strength (UTS) of the Q690 steel is 848 MPa, and the strain to failure is 13%. The UTS of the Q690 steel charged at 2 and 5 mA/cm^2 is 821 and 832 MPa, respectively, resulting in a slight elongation loss of 6.83% and 4.28%. The UTS and elongation at the break of the sample charged at 10 mA/cm^2 are 657 MPa and 3.32%, respectively. When hydrogen charging current density reached 50 mA/cm^2, the UTS and elongation were significantly degraded, reaching 570 MPa and 2.59%, respectively. During the hydrogen charging process, the HIB walls fall off the matrix and form cracks, which further lead to the reduction of the effective area to bear the load during the tensile process [43], and thus the reduction of the tensile strength. In addition, the easy depolymerization of blisters can also cause local stress concentration to activate HE. The performance degradation of the Q690 steel charged with hydrogen at different current densities is provided in Table S2 in the Supporting Information. The HE sensitivity gradually increases with the increase in the hydrogen charging current density (Figure 6c), providing evidence for hydrogen-assisted degradation. As the current density increases, the HE sensitivity of the steel increases more and more slowly. The hydrogen content in the matrix increases with the increase in current density. However, large hydrogen concentrations do not produce the expected increase in HE sensitivity as the hydrogen concentration saturates (Figure 6c). It is generally accepted by researchers that the SCC mechanism of low-alloy high-strength steel is dominated by anodic dissolution and hydrogen-induced cracking [44,45]. When charged at lower current densities, anodic dissolution remains effective and supports material failure. At high hydrogen charging current densities, hydrogen embrittlement dominates, and anodic dissolution hardly participates in the fracture process [46].

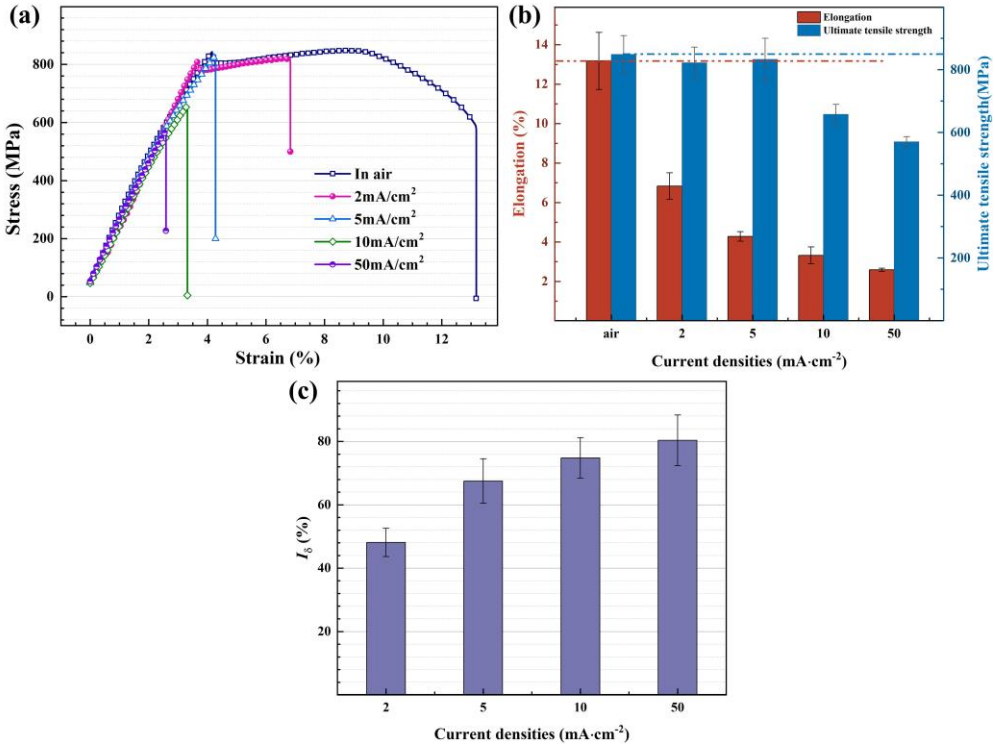

Figure 6. Stress–strain curves (**a**), ultimate tensile stress and elongation values (**b**), as well as HE susceptibility indexes in terms of elongation loss (**c**) of Q690 steel at different cathodic current densities.

3.2.2. Fractographic Analysis

Figure 7 provides the fracture morphologies of hydrogen-charged and non-hydrogen-charged samples. The surface of the uncharged sample shows obvious necking features (Figure 7a_1), which indicate that the Q690 steel has good ductility [47]. In addition, shear ridges, formed by shear deformation, and dimples of different sizes are observed (Figure 7a_2). The fracture characteristics belong to typical microporous aggregated ductile fractures.

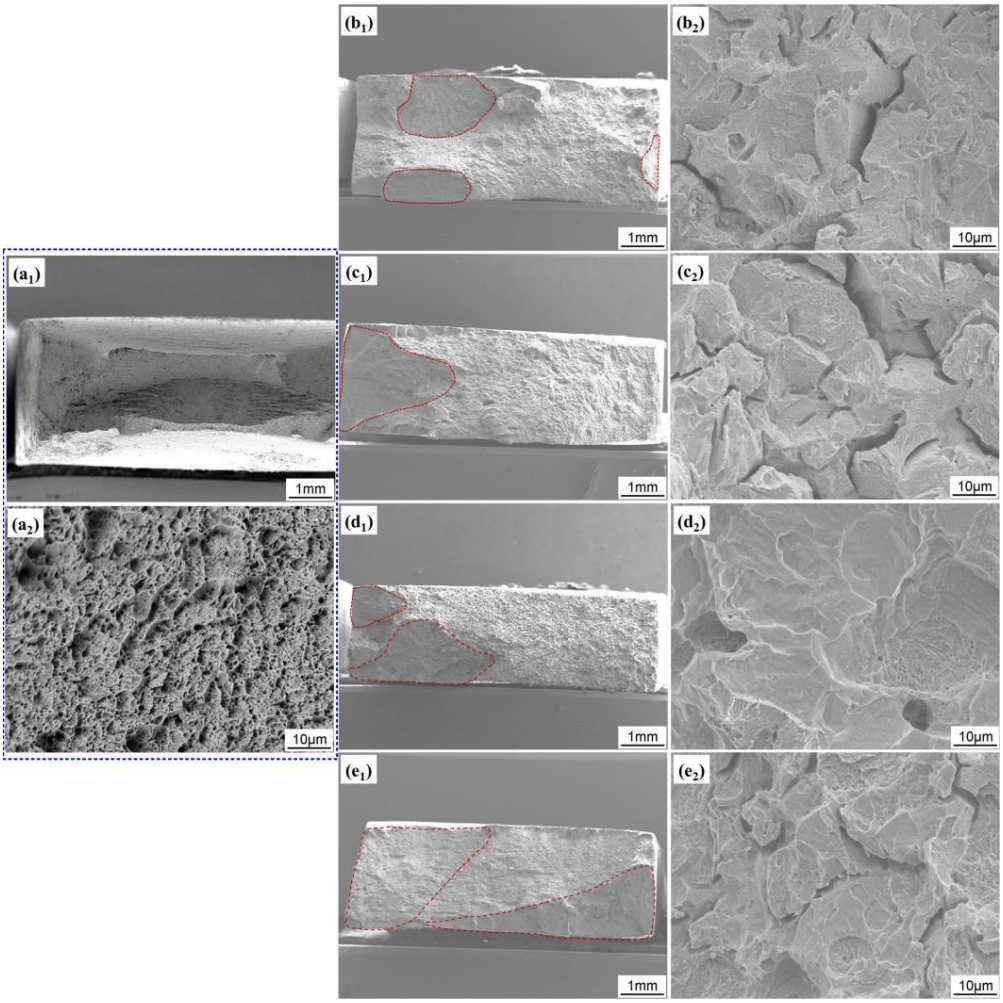

Figure 7. Morphologies of the fracture surfaces after the SSRT test for Q690 substrate under cathodic charging: (**a_1**,**a_2**) air, (**b_1**,**b_2**) 2 mA/cm^2, (**c_1**,**c_2**) 5 mA/cm^2, (**d_1**,**d_2**) 10 mA/cm^2, and (**e_1**,**e_2**) 50 mA/cm^2.

Brittle areas (marked by red dotted lines) appear on the fracture surface of all charged samples, and no obvious necking is found. When the hydrogen charging current is small (2, 5 mA/cm^2), the fracture presents the characteristics of dimple and quasi-cleavage mixed fracture, which can prove that brittle and ductile fractures occur simultaneously, and a large number of secondary cracks are observed on the fracture surface (Figure 7(b_1,b_2,c_1,c_2)). The effect of hydrogen on fracture is attributed to the accumulation of hydrogen at the matrix–particle interface, which reduces the interface strength. The fracture surface is mainly composed of the brittle crown region near the surface and the ductile region near the center (Figure 7(b_1,c_1)). With the further increase in the current density, the smooth brittle surface increases, and the brittle fracture gradually dominates the fracture of the charging steel (Figure 7(d_1,d_2,e_1,e_2)). The proportion of brittle regions further increases with the increase in the hydrogen charging current density (Figure 8). This further proves

that the toughness loss of the material increases, which is consistent with the change in the stress–strain curve mentioned above. After the application of the current, the fracture mode of the material changes from ductile necking to brittle fracture.

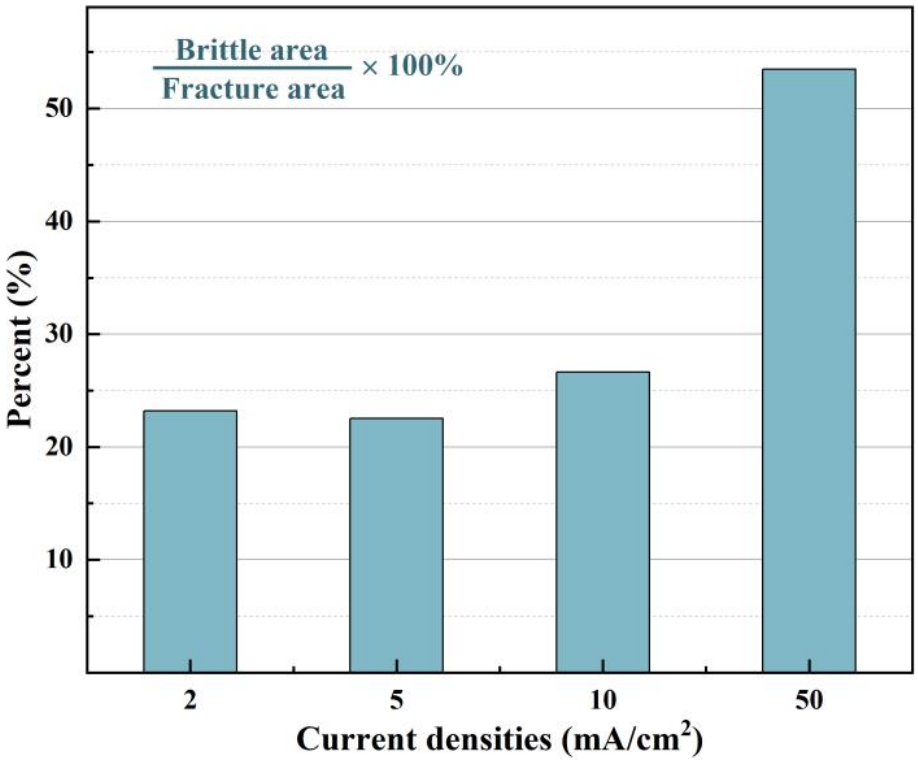

Figure 8. Brittle area fraction of Q690 steel under different current densities.

4. Conclusions

The relationship between charging conditions and hydrogen-assisted degradation of Q690 steel is investigated in this paper. The following conclusions are obtained:

(1) The current density has a significant effect on the blistering and internal damage of Q690 steel. As the current density increases, the shape of the blistering changes from dome shaped with well-defined boundaries to flat topped with rough edges, and the number of blisters increases accordingly.

(2) Compared with the growth of blisters, high current density is responsible for the initiation of blisters. At higher charging current densities (50 mA/cm^2) and longer charging time (12 h), deep hydrogen-induced cracks appear in the interior of the steel due to the mass accumulation of hydrogen at the boundary. As the hydrogen charging current density increases, the hydrogen-induced cracking mode changes from the intergranular and transgranular mixed mode to the intergranular mode.

(3) Electrochemical hydrogen charging causes the loss of mechanical properties of Q690 steel and the transition from ductile fracture to brittle fracture. The HE sensitivity and brittle zone area of Q690 steel increase with the increase in current density.

Supplementary Materials: The following supporting information can be downloaded at: https://www.mdpi.com/article/10.3390/cryst13060918/s1, Figure S1. Schematic diagram of the experimental setup for hydrogen charging used in hydrogen charging tests; Figure S2. Schematic diagram of the processing (a) and geometry (b) of tensile specimens used in SSRT tests as well as the schematic diagram of the experimental setup (c); Table S1. Relevant parameters of hydrogen charging experiments; and Table S2. Ultimate tensile strength, elongation, and energy density of Q690 alloy at different hydrogen charging current densities.

Author Contributions: Conceptualization, H.M., H.T., Z.W., K.H., Y.W. and Q.Z.; methodology, H.T., Y.W. and Q.Z.; validation, H.T. and Z.C.; formal analysis, H.M. and Z.W.; investigation, H.M., H.T., Z.W., K.H., Y.W., Q.Z. and D.L.; resources, Z.C.; data curation, D.L. and Z.C.; writing—original draft preparation, H.M. and H.T.; writing—review and editing, H.T.; visualization, D.L.; supervision, Z.C.; project administration, H.M. and Z.C.; funding acquisition, Z.C. All authors have read and agreed to the published version of the manuscript.

Funding: This research was funded by the 2021 Taishan industry leading talents project and the Key Research and Development Program of Shandong Province, grant number 2020CXGC010305.

Data Availability Statement: The raw/processed data required to reproduce these findings can be obtained when contacting the corresponding author.

Conflicts of Interest: The authors declare no conflict of interest.

References

1. Olsson, J.; Snis, M. Duplex—A new generation of stainless steels for desalination plants. *Desalination* **2007**, *205*, 104–113. [CrossRef]
2. Liu, D.; Cheng, B.; Chen, Y. Strengthening and toughening of a heavy plate steel for shipbuilding with yield strength of approximately 690 MPa. *Metall. Mater. Trans. A* **2013**, *44*, 440–455. [CrossRef]
3. Luo, H.; Zhao, B.; Pan, Z.; Fu, Y.; Li, X. Hydrogen induced microstructure evolution and cracking mechanism in a metastable dual-phase high-entropy alloy. *Mater. Sci. Eng. A* **2021**, *819*, 141490. [CrossRef]
4. Djukic, M.B.; Bakic, G.M.; Zeravcic, V.S.; Sedmak, A.; Rajicic, B. Hydrogen Embrittlement of Industrial Components: Prediction, Prevention, and Models. *Corrosion* **2016**, *72*, 943–961. [CrossRef] [PubMed]
5. Ćwiek, J. Prevention methods against hydrogen degradation of steel. *J. Achiev. Mater. Manuf. Eng.* **2010**, *43*, 214–221.
6. Zhou, C.; Tang, D.; Zhang, K.; Wu, F.; Lin, P.; Jin, Y.; Zhang, L.; Zheng, J. Effect of manganese content on the hydrogen embrittlement of twinning-induced plasticity (TWIP) steels under hydrogen charging and hydrogen environment. *Mater. Sci. Eng. A* **2022**, *861*, 144289. [CrossRef]
7. Tian, H.; Wang, X.; Cui, Z.; Lu, Q.; Wang, L.; Lei, L.; Li, Y.; Zhang, D. Electrochemical corrosion, hydrogen permeation and stress corrosion cracking behavior of E690 steel in thiosulfate-containing artificial seawater. *Corros. Sci.* **2018**, *144*, 145–162. [CrossRef]
8. Depover, T.; Wallaert, E.; Verbeken, K. Fractographic analysis of the role of hydrogen diffusion on the hydrogen embrittlement susceptibility of DP steel. *Mater. Sci. Eng. A* **2016**, *649*, 201–208. [CrossRef]
9. Venezuela, J.; Zhou, Q.; Liu, Q.; Zhang, M.; Atrens, A. Hydrogen Trapping in some automotive martensitic advanced high-strength steels. *Adv. Eng. Mater.* **2018**, *20*, 1700468. [CrossRef]
10. Ma, H.; Liu, Z.; Du, C.; Wang, H.; Li, C.; Li, X. Effect of cathodic potentials on the SCC behavior of E690 steel in simulated seawater. *Mater. Sci. Eng. A* **2015**, *642*, 22–31. [CrossRef]
11. Wu, S.; Gao, Z.; Liu, Y.; Hu, W. Effect of cathodic protection potential on stress corrosion susceptibility of X80 steel. *Corros. Sci.* **2023**, *218*, 111184. [CrossRef]
12. Tian, H.; Xin, J.; Li, Y.; Wang, X.; Cui, Z. Combined effect of cathodic potential and sulfur species on calcareous deposition, hydrogen permeation, and hydrogen embrittlement of a low carbon bainite steel in artificial seawater. *Corros. Sci.* **2019**, *158*, 108089. [CrossRef]
13. Deslouis, C.; Festy, D.; Gil, O.; Maillot, V.; Touzain, S.; Tribollet, B. Characterization of calcareous deposits in artificial sea water by impedances techniques: 2-deposit of $Mg(OH)_2$ without $CaCO_3$. *Electrochim. Acta* **2000**, *45*, 1837–1845. [CrossRef]
14. Barchiche, C.; Deslouis, C.; Festy, D.; Gil, O.; Refait, P.; Touzain, S.; Tribollet, B. Characterization of calcareous deposits in artificial seawater by impedance techniques: 3-deposit of $CaCO_3$ in the presence of Mg(II). *Electrochim. Acta* **2003**, *48*, 1645–1654. [CrossRef]
15. Simoni, L.; Caselani, J.Q.; Ramos, L.B.; Schroeder, R.M.; Malfatti, C.; de Fraga, C. The influence of calcareous deposits on hydrogen uptake and embrittlement of API 5CTP110 steel. *Corros. Sci.* **2017**, *118*, 178–189. [CrossRef]
16. Zhang, L.; Shen, H.-J.; Sun, J.-Y.; Sun, Y.-N.; Fang, Y.-C.; Cao, W.-H.; Xing, Y.-Y.; Lu, M.-X. Effect of calcareous deposits on hydrogen permeation in X80 steel under cathodic protection. *Mater. Chem. Phys.* **2018**, *207*, 123–129. [CrossRef]
17. Li, X.; Huang, W.; Wu, X.; Zhang, J.; Wang, Y.; Akiyama, E.; Hou, D. Effect of hydrogen charging time on hydrogen blister and hydrogen-induced cracking of pure iron. *Corros. Sci.* **2021**, *181*, 109200. [CrossRef]
18. Wang, S.; Xu, D.K.; Zhang, Z.Q.; Ma, Y.J.; Qiao, Y.X. Effect of electrochemical hydrogen charging on the mechanical behavior of a dual-phase Ti–4Al–2V–1Mo–1Fe (in wt.%) alloy. *Mater. Sci. Eng. A* **2021**, *802*, 140448. [CrossRef]
19. Xing, Y.; Yang, Z.; Yao, X.; Wang, X.; Lu, M.; Zhang, L.; Qiao, L. Effects of hydrogen on the fracture toughness of X80 steel base metal and girth weld under strong cathodic current with in-situ hydrogen charging. *Eng. Fail. Anal.* **2022**, *135*, 106143. [CrossRef]
20. Mohtadi-Bonab, M.A.; Szpunar, J.A.; Razavi-Tousi, S.S. A comparative study of hydrogen induced cracking behavior in API 5L X60 and X70 pipeline steels. *Eng. Fail. Anal.* **2013**, *33*, 163–175. [CrossRef]
21. Zhang, L.; Shen, H.; Lu, K.; Cao, W.; Sun, Y.; Fang, Y.; Xing, Y.; Du, Y.; Lu, M. Investigation of hydrogen concentration and hydrogen damage on API X80 steel surface under cathodic overprotection. *Int. J. Hydrogen Energy* **2017**, *42*, 29888–29896. [CrossRef]

22. Dunne, D.P.; Hejazi, D.; Saleh, A.A.; Haq, A.; Calka, A.; Pereloma, E. Investigation of the effect of electrolytic hydrogen charging of X70 steel: I. The effect of microstructure on hydrogen-induced cold cracking and blistering. *Int. J. Hydrogen Energy* **2016**, *41*, 12411–12423. [CrossRef]
23. Ghosh, G.; Rostron, P.; Garg, R.; Panday, A. Hydrogen induced cracking of pipeline and pressure vessel steels: A review. *Eng. Fract. Mech.* **2018**, *199*, 609–618. [CrossRef]
24. Escobar, D.P.; Miñambres, C.; Duprez, L.; Verbeken, K.; Verhaege, M. Internal and surface damage of multiphase steels and pure iron after electrochemical hydrogen charging. *Corros. Sci.* **2011**, *53*, 3166–3176. [CrossRef]
25. Ren, X.; Chu, W.; Li, J.; Su, Y.; Qiao, L. The effects of inclusions and second phase particles on hydrogen-induced blistering in iron. *Mater. Chem. Phys.* **2008**, *107*, 231–235. [CrossRef]
26. Balden, M.; Lindig, S.; Manhard, A.; You, J.-H. D2 gas-filled blisters on deuterium-bombarded tungsten. *J. Nucl. Mater.* **2011**, *414*, 69–72. [CrossRef]
27. Hoshihira, T.; Otsuka, T.; Tanabe, T. Visualization of hydrogen distribution around blisters by tritium radio-luminography. *J. Nucl. Mater.* **2009**, *386–388*, 776–779. [CrossRef]
28. Tiegel, M.C.; Martin, M.L.; Lehmberg, A.K.; Deutges, M.; Borchers, C.; Kirchheim, R. Crack and blister initiation and growth in purified iron due to hydrogen loading. *Acta Mater.* **2016**, *115*, 24–34. [CrossRef]
29. Garofalo, F.; Chou, Y.T.; Ambegaokar, V. Effect of hydrogen on stability of micro cracks in iron and steel. *Acta Metall.* **1960**, *8*, 504–512. [CrossRef]
30. Pan, Z.; Wei, Y.; Fu, Y.; Luo, H.; Li, X. Effect of electrochemical hydrogen charging on the mechanical property and corrosion behavior of Ti-3Mo alloy. *Corros. Sci.* **2022**, *200*, 110219. [CrossRef]
31. Lu, X.; Wang, D.; Wan, D.; Zhang, Z.B.; Kheradmand, N.A. Barnoush Effect of electrochemical charging on the hydrogen embrittlement susceptibility of alloy 718. *Acta Mater.* **2019**, *179*, 36–48. [CrossRef]
32. Wang, L.; Liang, J.; Li, H.; Cheng, L.; Cui, Z. Quantitative study of the corrosion evolution and stress corrosion cracking of high strength aluminum alloys in solution and thin electrolyte layer containing Cl. *Corros. Sci.* **2021**, *178*, 109076. [CrossRef]
33. Kamoutsi, H.; Haidemenopoulos, G.N.; Bontozoglou, V.; Pantelakis, S. Corrosion-induced hydrogen embrittlement in aluminum alloy 2024. *Corros. Sci.* **2006**, *48*, 1209–1224. [CrossRef]
34. Tao, X.; Lv, G.-C.; Kou, J.; Xiong, X.; Volinsky, A.A.; Ku, C.-S.; Chen, K.; Su, Y.-J. Synchrotron X-ray Laue diffraction study of hydrogen-induced blisters on iron grain boundaries. *Scr. Mater.* **2019**, *169*, 82–86. [CrossRef]
35. Zhang, S.; Zhao, Q.; Liu, J.; Huang, F.; Huang, Y.; Li, X. Understanding the effect of niobium on hydrogen-induced blistering in pipeline steel: A combined experimental and theoretical study. *Corros. Sci.* **2019**, *159*, 108142. [CrossRef]
36. Perng, T.P.; Wu, J.K. A brief review note on mechanisms of hydrogen entry into metals. *Mater. Lett.* **2003**, *57*, 3437–3438. [CrossRef]
37. Chu, W.Y. *Hydrogen Embrittlement and Stress Corrosion*; Science Press: Beijing, China, 2013.
38. Santos, L.; Béreš, M.; Bastos, I.; Tavares, S.; Abreu, H.; da Silva, M.G. Hydrogen embrittlement of ultra high strength 300 grade maraging steel. *Corros. Sci.* **2015**, *101*, 12–18. [CrossRef]
39. Wang, S.; Martin, M.L.; Sofronis, P.; Ohnuki, S.; Hashimoto, N.; Robertson, I.M. Hydrogen-induced intergranular failure of iron. *Acta Mater.* **2014**, *69*, 275–282. [CrossRef]
40. Wang, S.; Martin, M.L.; Robertson, I.M.; Sofronis, P. Effect of hydrogen environment on the separation of Fe grain boundaries. *Acta Mater.* **2016**, *107*, 279–288. [CrossRef]
41. Nagao, A.; Dadfarnia, M.; Somerday, B.P.; Sofronis, P.; Ritchie, R.O. Hydrogen-enhanced-plasticity mediated decohesion for hydrogen-induced intergranular and"quasi-cleavage" fracture of lath martensitic steels. *J. Mech. Phys. Solids* **2018**, *112*, 403–430. [CrossRef]
42. Chen, Y.; Zhang, T.; Song, L. Hydride formation during cathodic charging and its effect on mechanical properties of a high Nb containing TiAl alloy. *Int. J. Hydrogen Energy* **2018**, *43*, 8161–8169. [CrossRef]
43. Singh, V.; Singh, R.; Arora, S.K.; Mahajan, D.K. Hydrogen induced blister cracking and mechanical failure in X65 pipeline steels. *Int. J. Hydrogen Energy* **2019**, *44*, 22039–22049. [CrossRef]
44. Wu, W.; Wang, Q.; Yang, L.; Liu, Z.; Li, X.; Li, Y. Corrosion and SCC initiation behavior of low-alloy high-strength steels microalloyed with Nb and Sb in a simulated polluted marine atmosphere. *J. Mater. Res. Technol.* **2020**, *9*, 12976–12995. [CrossRef]
45. Liu, Z.Y.; Li, X.G.; Cheng, Y.F. Mechanistic aspect of near-neutral pH stress corrosion cracking of pipelines under cathodic polarization. *Corros. Sci.* **2012**, *55*, 54–60. [CrossRef]
46. Fan, E.; Zhao, Q.; Wang, S.; Liu, B.; Yang, Y.; Huang, Y.; Luo, H.; Li, X. Investigation of the hydrogen-induced cracking of E690 steel welded joint in simulated seawater. *Mater. Sci. Eng. A* **2022**, *854*, 143802. [CrossRef]
47. Xing, X.; Cheng, R.; Cui, G.; Liu, J.; Gou, J.; Yang, C.; Li, Z.; Yang, F. Quantification of the temperature threshold of hydrogen embrittlement in X90 pipeline steel. *Mater. Sci. Eng. A* **2021**, *800*, 140118. [CrossRef]